corrosion and materials degradation

MDPI

Article

Hydrogen Embrittlement Resistance of an Optimized Additively Manufactured Austenitic Stainless Steel from Recycled Sources

Mattia Cabrioli [1,*], María Silva Colmenero [1], Matteo Vanazzi [1], Luisa E. Mondora [1,2], Gianluca Acquistapace [2], Fabio Esposito [3] and Michela Giovanardi [3]

[1] f3nice, Via Roccoli, 252, 23010 Piantedo, SO, Italy; maria.silva@f3nice.com (M.S.C.); matteo.vanazzi@f3nice.com (M.V.); luisa.mondora@valland.it (L.E.M.)
[2] Valland SpA, Via Roccoli, 252, 23010 Piantedo, SO, Italy; gianluca.acquistapace@valland.it
[3] TEC Eurolab S.r.l, Viale Europa, 40, 41011 Campogalliano, MO, Italy; esposito@tec-eurolab.com (F.E.); giovanardi@tec-eurolab.com (M.G.)
* Correspondence: mattia.cabrioli@f3nice.com

Abstract

In the framework of hydrogen production and storage for clean energy generation, the resistance to hydrogen embrittlement of a newly developed austenitic stainless steel is presented. Gas-atomized metal powders prepared from secondary-sourced metals were employed to manufacture test specimens with Laser Powder Bed Fusion (LPBF) technology. After machining and exposure to a controlled, pressurized hydrogen atmosphere at high temperature, the effect of hydrogen charging on the mechanical performance under static and dynamic conditions was investigated. The stabilizing effect of the optimized chemical composition is reflected in the absence of degradation effects on Yield Stress (YS), Ultimate Tensile Stress (UTS), and fatigue life observed for specimens exposed to hydrogen. Moreover, despite a moderate reduction in the elongation at fracture observed by increasing the hydrogen charging time, ductility loss calculated as Relative Reduction of Area (RRA) remains substantially unaffected by the duration of exposure to hydrogen and demonstrates that the austenitic steel is capable of resisting hydrogen embrittlement (HE).

Keywords: hydrogen embrittlement resistance; stainless steel; additive manufacturing (AM); laser powder bed fusion (LPBF); metal recycling

Academic Editor: Kevin Ogle

Received: 13 June 2025
Revised: 12 July 2025
Accepted: 18 July 2025
Published: 26 July 2025

Citation: Cabrioli, M.; Silva Colmenero, M.; Vanazzi, M.; Mondora, L.E.; Acquistapace, G.; Esposito, F.; Giovanardi, M. Hydrogen Embrittlement Resistance of an Optimized Additively Manufactured Austenitic Stainless Steel from Recycled Sources. *Corros. Mater. Degrad.* **2025**, *6*, 34. https://doi.org/10.3390/cmd6030034

1. Introduction

In the global effort towards reduction of carbon emissions and mitigation of climate change, hydrogen is one of the key assets to pursue worldwide sustainability goals [1]. The chemical and physical properties of hydrogen gas make it a versatile vector for energy transport, storage, and management, alongside conferring suitable characteristics as fuel for generating clean energy with near-to-zero emissions to the environment.

Nonetheless, despite the potential benefits associated with hydrogen, technical issues currently hinder the deployment of an effective and reliable hydrogen value chain: production based on electrolyzers, storage, distribution, and consumption in fuel cells are still affected by material compatibility issues [2]. Corrosion and embrittlement phenomena have limited the applicability of traditionally used materials, specifically concerning

metals and their alloys, as structural and critical components [3]. Corrosion issues due to harsh environmental conditions related to either strongly acidic or basic environments are typical of electrolyzer technology [4,5], whereas temperature plays a fundamental role in the field of fuel cells [6,7]. At the same time, hydrogen embrittlement (HE) may degrade the mechanical performance of metallic components, especially pipelines and vessels present in the storage and distribution sectors, leading to enhanced cracking susceptibility and eventually resulting in catastrophic failures [3].

Mechanisms governing HE are complex and typically related to internal and external factors such as materials and microstructures, stress state, and environmental parameters. In particular, various modes have been identified with regard to the pathway from hydrogen entering a metal component, to promoting internal changes, and eventually leading to failure. Among them, the main mechanisms are hydrogen-enhanced decohesion (HEDE), hydrogen-induced phase transformation (HIPT), hydrogen-enhanced local plasticity (HELP), hydrogen-enhanced strain-induced vacancy (HESIV), and adsorption-induced dislocation emission (AIDE) [3,8]. Despite giving a comprehensive understanding of the internal changes caused by hydrogen, these physical models must still be complemented by experimental assessment of the mechanical performance in the presence of hydrogen to give a reliable indication of the resistance to HE of the candidate materials for hydrogen service.

Various metals, polymers, and composite materials have been studied and tested for hydrogen applications [3,9,10]. The class of iron-based alloys has been identified as most suitable for use as structural materials. In particular, austenitic steels are deemed to exhibit the highest resistance to HE, due to solubility of hydrogen in their FCC crystalline structure, and with a performance related to the stability of the austenite phase [3,11].

In this field, the chemical composition and microstructure of the alloy further affect the mechanical performance in the presence of hydrogen. The resistance of austenite to transformation into martensite phases, which are more susceptible to HE, could be predicted by means of descriptors such as the nickel-equivalent content (Ni_{eq}) and Stacking Fault Energy (SFE). The first one is based on a simple equation that considers the concentration of austenitizing elements on the alloy to estimate the HE, whereas the second one accounts for intrinsic thermodynamic properties of the crystalline structure in terms of austenite to martensite transformation and their interactions with dislocations [12,13]. It has been reported that the major impact on austenitic stabilization is given by nickel (Ni) concentration in the stainless steel, which increases the SFE value, whereas molybdenum (Mo) could be considered as a moderate austenite stabilizer, and high chromium (Cr) contents are generally preferable to ensure good corrosion resistance [9,14,15].

In combination with the local chemical environment, metallurgical features characterizing the microstructure of metal alloys also play a significant role in determining HE susceptibility. The grain size and orientation, the nature and distribution of precipitates, and the defects of the crystalline lattice all interact with hydrogen atoms and contribute to the well-known HE mechanisms [16–18]. Processing parameters such as solidification rate can be tuned in order to obtain tailored microstructural features and defects of the crystalline lattice, such as dislocations. If properly controlled, those could be used as trapping sites for hydrogen atoms and thus decrease HE susceptibility. Therefore, recent investigations have focused on the effects of the peculiar solidification structures derived from the Additive Manufacturing (AM) of stainless steels, which may offer advantageous features in the AM material with respect to their counterpart by a conventional route by virtue of the density and distribution of dislocations that effectively slow down the diffusion of hydrogen atoms [19–27].

Specifically, a limited number of research groups evaluated the effects of HE on 316L material manufactured by Laser Powder Bed Fusion (LPBF) technology, as reported in

recent comparative studies and reviews [23,25]. By comparing the tensile properties of the material with or without hydrogen charging, it was possible to highlight appreciable changes in tensile strength and ductility. Although not always consistent throughout the scientific literature, the most observed general behavior is that of reduced ductility of pre-charged specimens. Considering either the Reduction of Area due to necking of the metal subjected to tensile load, or the elongation at fracture, the measured values of these properties are typically lowered due to the presence of hydrogen. Despite deeper knowledge having been provided regarding the fundamental mechanisms of HE, some differences still remain in the experimental results, mainly due to significant changes in the process parameters for hydrogen pre-charging, namely the methodology (electrochemical or thermally assisted gaseous charging), charging current, environmental temperature, hydrogen pressure, and duration of charging step. Moreover, a direct comparison of different results should also take into account the synergistic effects of chemical composition and microstructure of the AM materials, making it even more difficult to build a reference for future research work.

In this study, the chemical composition of an austenitic stainless steel of the 316 family was tuned to aim for stabilization of the mechanical performance of the alloys in hydrogen-rich environments. Starting from 316L scrap metal, chemical composition has been enhanced by the addition of specific alloying elements, such as Ni, Cr, and Mo, to improve the resistance to HE. With this reference, powders atomized by gas atomization from secondary-sourced metals were used as feedstock for printing test specimens with LPBF. The tensile strength and fatigue life were then evaluated before and after exposure to thermal hydrogen charging conditions. The results of the investigations presented in this paper highlight the excellent resistance to hydrogen-induced embrittlement for the additively manufactured austenitic stainless steel with optimized chemical composition.

2. Materials and Methods

2.1. Scrap Material Sourcing and Preparation

In order to obtain the customized alloy designed, austenitic stainless steel 316L was employed as the base material. Secondary-sourced 316L scrap, comprising obsolete components and leftovers from machining, was collected and selected for processing. The material was melted in a Vacuum Induction Melting (VIM) furnace (ALD Vacuum Technologies, Hanau, Germany). Targeted alloying elements—specifically chromium, nickel, and molybdenum—were introduced to adjust the chemical composition of the melt towards targeted values.

Following the melting process and compositional adjustments, the alloy was cast into ingots to be used as feedstock in the gas atomization process.

2.2. Powder Atomization and Characterization

The gas atomization process was carried out using a laboratory-scale Vacuum Inert Gas Atomizer (VIGA) (ALD Vacuum Technologies, Hanau, Germany). The pre-processed metal feedstock was melted by an induction coil, in a refractory crucible that was heated to 1750 °C, under an inert atmosphere of nitrogen gas at a controlled pressure of 0.5 bar. The liquid metal was poured into a preheated nozzle, where it was broken down by an inert gas jet of 30–60 bar at 500 °C, thus forming droplets that detached from the liquid phase and solidified into micrometer-sized spherical powder.

The resulting powder was subjected to a sieving procedure inside a glove box, using a cyclone separator system working under inert conditions.

Comprehensive characterization of the atomized metal powder was conducted to evaluate its suitability for LPBF applications. Chemical composition of the metal powders

was analyzed by Inductively Coupled Plasma Optical Emission Spectroscopy (ICP-OES) (LECO, Saint Joseph, MI, USA). Morphological analysis was performed using scanning electron microscopy (SEM) (TESCAN, Kohoutovice, Czech Republic). Particle size distribution (PSD) was measured by laser diffraction-based analysis (Malvern Panalytical, Malvern, United Kingdom) in accordance with ISO 13320:2020 standard [28].

Apparent density and tap density were measured according to ASTM B212 [29] and ASTM B527 [30], respectively, using a Hall funnel (Bettersize, Liaoning, China) and an automatic tap density device (Bettersize, Liaoning, China). Flowability was further evaluated through Hall flow rate testing according to ASTM B213 [31] standards.

2.3. Printing of Atomized Powders and Preparation of Test Specimens

Specimens for mechanical testing were fabricated using LPBF on a standard EOS M290 system(EOS, Krailing, Germany). Standard process parameters for Stainless Steel 316L were used during printing, because of the compositional alignment with the customized alloy. The printing process was performed under an inert atmosphere, using a layer thickness of 40 μm, a laser power of 370 W, a scan speed of 1200 mm/s, a hatch distance of 0.10 mm, and a 'chessboard' pattern scanning strategy.

Following printing, the samples were machined to conform with ASTM E8 [32] for tensile testing and ASTM E466 [33] for fatigue testing, while planar control samples were used to assess the concentration of absorbed hydrogen.

2.4. Testing Mechanical Performance and Resistance to Hydrogen Embrittlemen

The experimental matrix presented in Table 1 was designed to simulate the aging process affecting metallic components in hydrogen-rich environments, aiming to evaluate the influence of internal hydrogen, resulting from prolonged hydrogen exposure, on the material's fatigue resistance and tensile properties. Hydrogen pre-charging was conducted under controlled conditions at a pressure of 100 bar and a temperature of 300 °C.

Table 1. Test matrix for simulating hydrogen aging on customized stainless steel specimens.

Test Type	Condition	No. of Specimens
High Cycle Fatigue (HCF)	As-machined [1]	3
	Pre-charged—360 h	3
Tensile Test	As-machined [1]	4
	Pre-charged—120 h	4
	Pre-charged—360 h	4
Hydrogen content	As-machined [1]	1
	Pre-charged—120 h	1
	Pre-charged—360 h	1

[1] Pre-charging was not performed.

Figure 1 shows the aging process applied to the printed samples to simulate their exposure to hydrogen-rich environments, with the goal of investigating the impact of prolonged hydrogen exposure on the material's properties. Panel (a) displays the autoclave equipment used for pre-charging in hydrogen at 100 bar and 300 °C, while panel (b) shows the sample holder to be mounted inside the controlled environment of the charging setup.

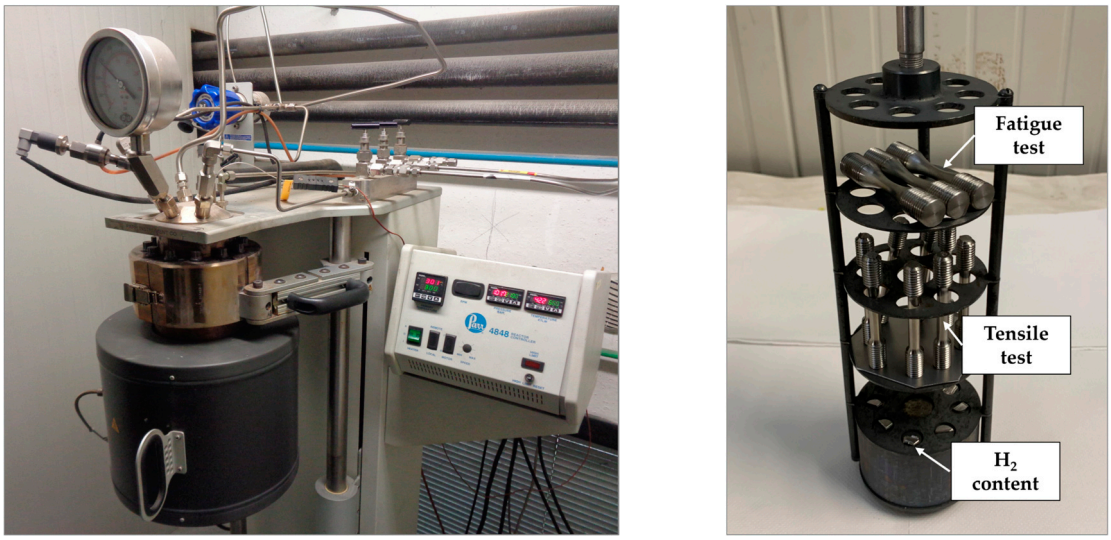

(**a**) (**b**)

Figure 1. Aging process simulated to investigate the impact of prolonged hydrogen exposure of AM Stainless Steel: (**a**) autoclave equipment used for pre-charging in hydrogen, and (**b**) sample holder to be inserted in the pre-charging setup, with specimens for fatigue and tensile tests, and measurement of hydrogen content.

Mechanical properties of both the as-machined and pre-charged conditions were measured. Static properties were assessed through tensile testing in accordance with ASTM E8 [32], and fatigue tests followed the ASTM E466 [33] standard. The hydrogen content absorbed in the specimens was measured by means of inert gas fusion (LECO, Saint Joseph, MI, USA). All mechanical testing was performed at room temperature. Fractographic observations were conducted by both SEM and Optical Microscopy (OM) (ZEISS, Oberkochen, Germany).

3. Results

3.1. Optimization of Chemical Composition

Table 2 presents the evolution of the chemical composition throughout the production process, from secondary-sourced 316L metal to the VIGA atomized powders.

Table 2. Optimization of chemical composition in the 316L material, from scrap to powder.

Element	Metal Scrap 316L [wt. %]	Target Composition [wt. %]	Atomized Powder [wt. %]
Fe	Balance	Balance	Balance
Cr	16.80	17.00–19.00	18.0
Ni	10.17	13.00–15.00	13.9
Mo	2.07	2.25–3.00	2.63
C	0.02	<0.03	0.027
Mn	1.7	<2.00	1.13
Cu	0.40	<1.00	0.44
P	0.03	<0.045	0.028
S	0.02	<0.030	0.014
Si	0.34	<1.00	0.36
N	0.06	<0.10	0.04
O	N/A *	<0.10	0.027

* N/A (not assessed).

The composition of the stainless steel scrap served as a starting point. Specifically, the following values were measured for three key elements in the 316L: Cr (16.80 wt.%), Ni (10.17 wt.%), and Mo (2.07 wt.%). During the VIM process, targeted alloying adjustments were implemented to enhance corrosion resistance and mechanical response of the alloy in hydrogen-rich environments, as previously noted from the literature findings. Here, Cr, Ni, and Mo were increased reaching levels such as Cr (18.0 wt.%), Ni (13.9 wt.%), and Mo (2.63 wt.%) in the atomized powder, in accordance with target composition levels reported in Table 2. In addition, minor reductions in some of the well-known impurities were detected, reflecting the enhancement in purity due to the VIGA process.

3.2. Characterization of Powders Atomized from Scrap Metal

The particle size distribution (PSD) of the atomized metal powder within the 20–63 μm size range was measured by laser diffraction-based analysis. The resulting PSD exhibited a unimodal profile, with the key percentile values determined as D10 = 20.9 μm, D50 = 34.3 μm, and D90 = 55.2 μm, confirming a well-centered distribution. Physical properties such as apparent density, tap density, and flowability were evaluated and the resulting properties are reported in Table 3:

Table 3. Hall flowability, apparent density, and tap density values for 316L-customized powders.

Hall Flowability [s/75 g]	Apparent Density [g/cm³]	Tap Density [g/cm³]
15.5	4.1	4.8

Concerning the morphology of the particles, SEM images reported in Figure 2 showed that the powders presented adequate sphericity, according to the characteristics of the VIGA atomization process. The presence of elongated particles, satellites, or agglomerates was limited, suggesting an optimal processability.

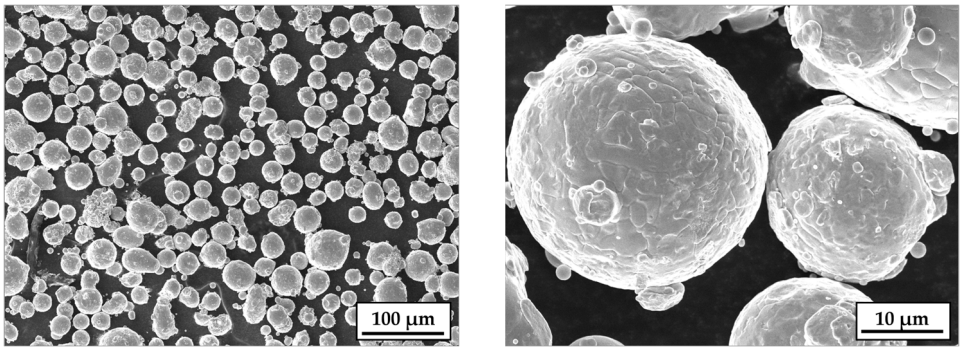

(**a**) (**b**)

Figure 2. SEM images of the atomized 20–63 μm fraction powders, observed at (**a**) lower and (**b**) higher magnification.

3.3. Effect of Hydrogen Loading on Mechanical Properties of AM Stainless Steel

Hydrogen content was assessed by means of inert gas fusion on plate-shaped specimens representative of both the as-machined and pre-charged conditions. Due to limited available space in the aging chamber where hydrogen charging was conducted, only one sample was used for each condition. The results, summarized in Table 4, indicated a significant increase in hydrogen content of the specimens pre-charged for 120 h and 360 h. Moreover, it appears that a plateau condition is reached after 120 h, since the hydrogen content is not varying significantly by exposing the stainless steel for three times longer duration.

Table 4. Results of inert gas fusion analysis on as-machined and pre-charged specimens.

	As-Machined [1]	Pre-Charged for 120 h	Pre-Charged for 360 h
Hydrogen content [ppm]	1.2 ± 0.7	40.4 ± 6.8	36.8 ± 6.1

[1] Pre-charging was not performed.

This increase moderately affected the mechanical properties, supporting the hypothesis that hydrogen atoms altered the material's microstructure sufficiently to see minor changes in its mechanical response.

Table 5 shows the tensile test results for customized stainless steel samples. Each value shown corresponds to the average of the four measurements for each condition. The associated extended uncertainty (U) is calculated at a 95% confidence level using a coverage factor k = 2, based on the standard deviation of the measurements.

Table 5. Tensile test results of non-charged and hydrogen pre-charged samples.

Condition	UTS [MPa]	YS [MPa]	E_f [%]	Ψ [%]
As-machined [1]	559.5 ± 2.0	464.0 ± 7.1	43.5 ± 2.7	63.5 ± 6.6
Pre-charged 120 h	564.5 ± 4.2	465.0 ± 7.7	39.1 ± 5.3	62.8 ± 5.3
Pre-charged 360 h	569.3 ± 3.8	472.3 ± 9.9	35.5 ± 5.3	65.0 ± 3.7

[1] Pre-charging was not performed.

The following mechanical properties were determined during the test: Ultimate Tensile Stress (UTS), Yield Stress (YS), elongation at fracture (E_f), and Reduction of Area (Ψ). The tensile Stress–Strain (σ-ε) diagrams for pre-charged and non-charged specimens are shown in Figure 3 as the result of an averaging process of four specimens for each condition.

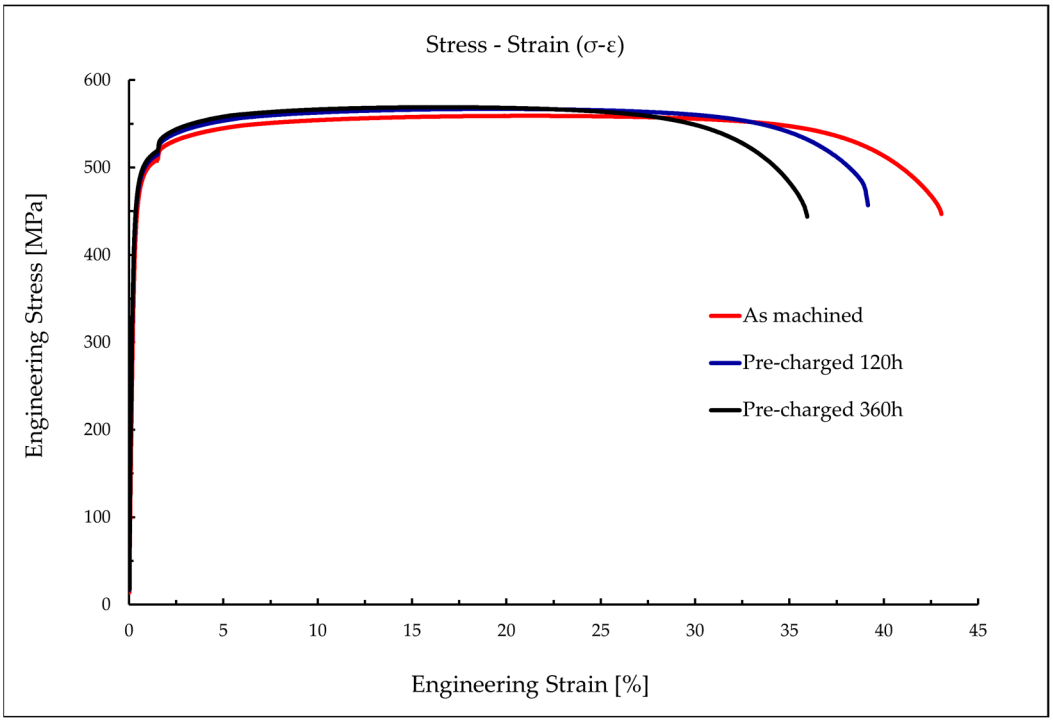

Figure 3. Stress–Strain (σ-ε) diagrams for pre-charged and non-charged specimens.

Hydrogen charging causes a change in the mechanical properties of the specimens, as shown in Figure 3. Hydrogen impacted on the strength of the material by increasing both the Yield and Tensile Stress. The reduction in elongation at fracture was consistent and revealed a moderate loss of ductility under hydrogen exposure. On the other hand, values of the Reduction of Area were statistically similar for specimens under as-machined and pre-charged conditions.

Fractographic examination completed the analysis of fractured specimens to gain deeper insight into the role of hydrogen in the modification of mechanical properties of AM-customized stainless steel. An overview of all the tested conditions is included in Figure 4, where SEM and OM observations are shown for exemplary specimens of each condition:

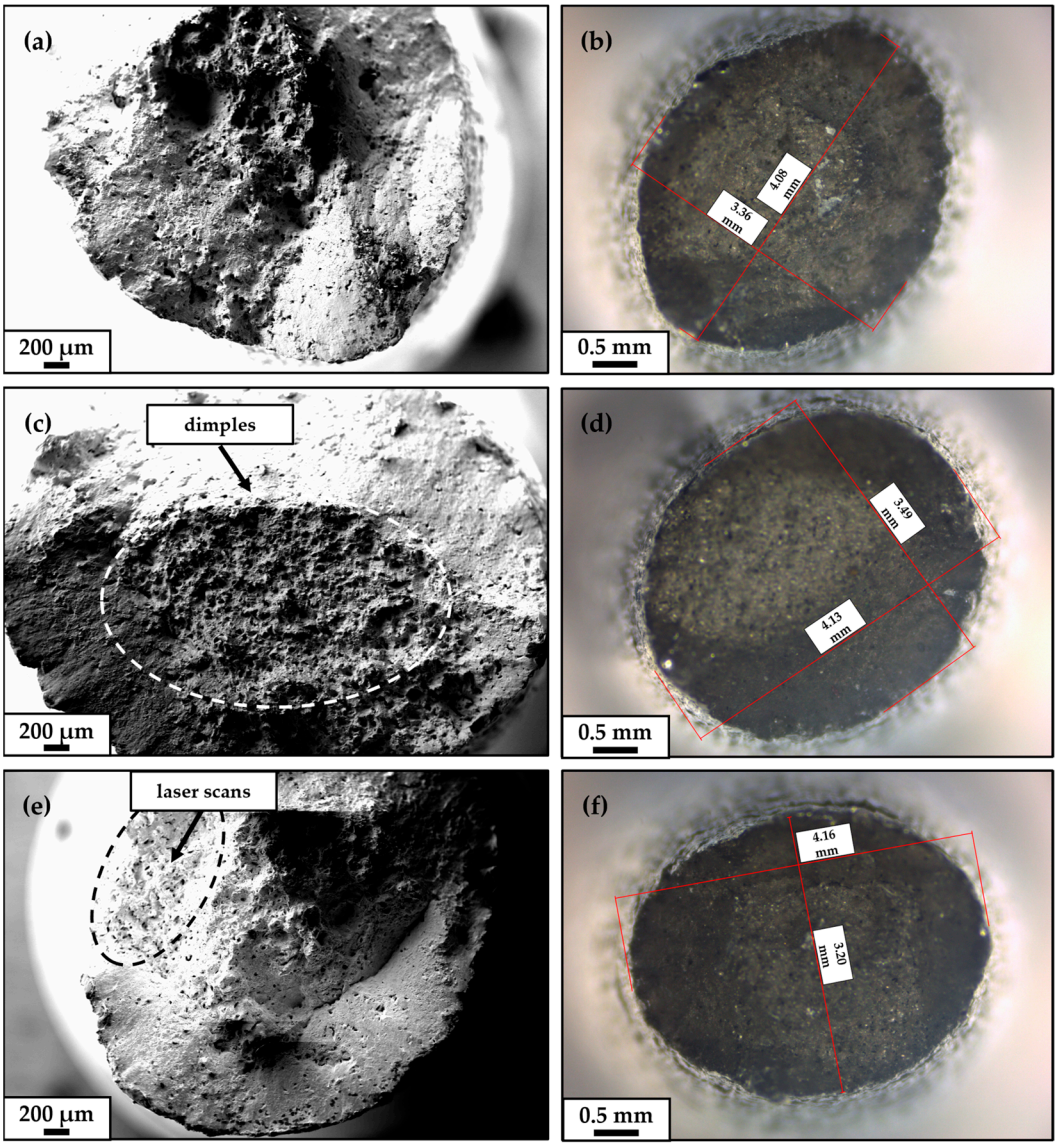

Figure 4. Fracture surfaces of specimens after tensile tests. SEM micrographs and OM views of fractured specimens are shown for (**a**,**b**) as-machined condition, (**c**,**d**) pre-charged at 100 bar and 300 °C for 120 h, and (**e**,**f**) pre-charged at 100 bar and 300 °C for 360 h.

The fatigue stress response of the as-machined and pre-charged for 360 h samples was evaluated by High Cycle Fatigue (HCF) testing, with three samples for each condition. The tests were carried out at room temperature, under axial loading with a stress ratio of 0.1—i.e., the ratio of minimum and maximum applied stresses—and sinusoidal

wave form at a frequency of 99 Hz. Failure was observed for all tested samples in order of 10^5 cycles. The results are reported in Table 6.

No degradation was induced by hydrogen exposure of the metallic specimens. Indeed, the fatigue strength was increased in samples subjected to a hydrogen-rich environment. Fractographic examination was performed on the specimens with the highest fatigue strength behavior. Figure 5 shows the fracture surface after fatigue testing. The right-hand column (a,b,c,d) shows the results obtained for the as-machined sample, while the left-hand column (e,f,g,h) shows the results for the sample subjected to 360 h of hydrogen aging.

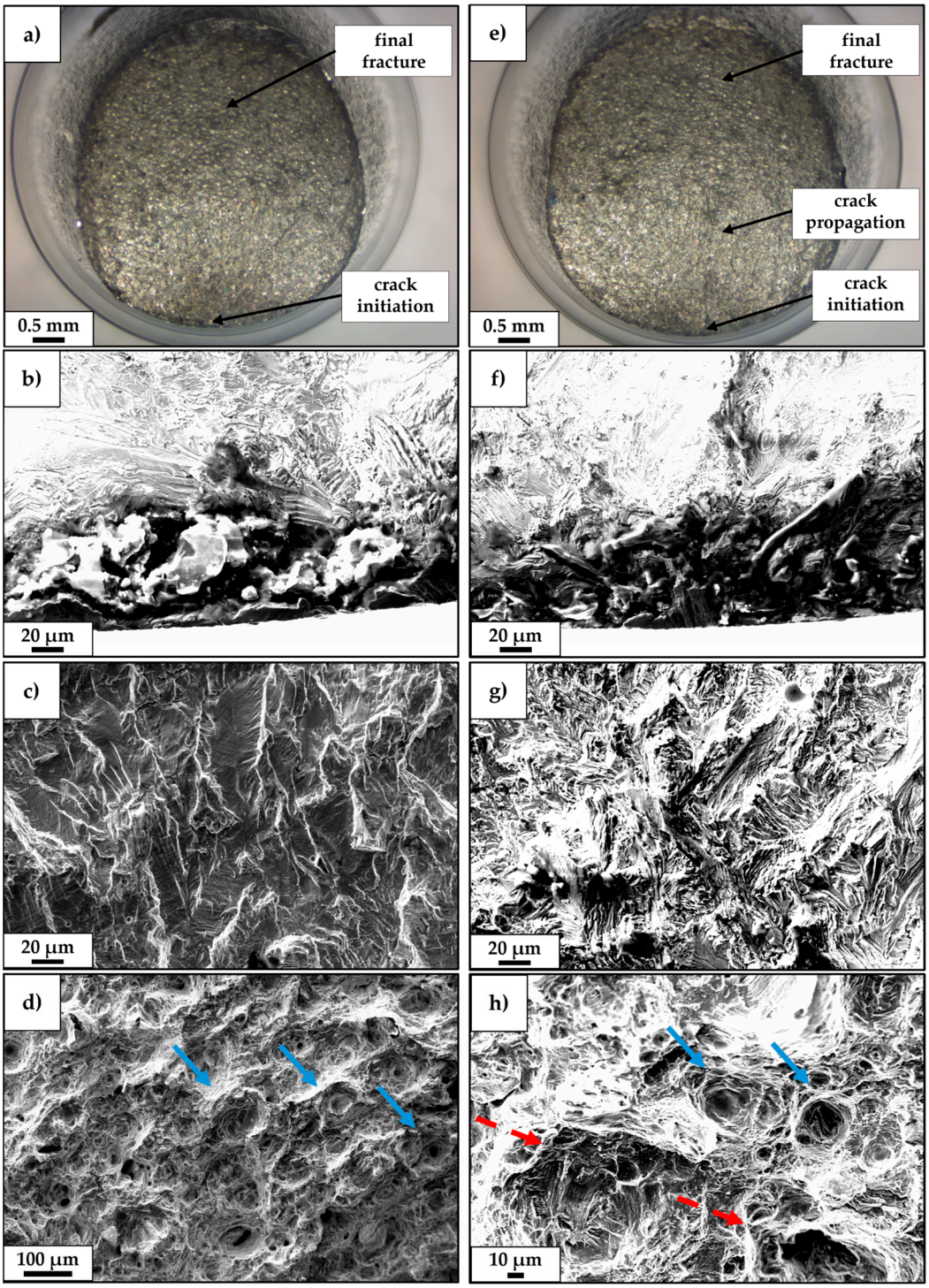

Figure 5. Fracture surfaces of specimens after fatigue tests. OM views of fractured specimens are shown for (**a**) $N_f = 5.0 \times 10^5$ cycles and (**e**) $N_f = 4.1 \times 10^5$ cycles. SEM images of (**b**,**f**) crack initiation

sites, (**c**,**g**) crack propagation, and (**d**,**h**) final fracture features are presented. Presence of dimples (blue arrows) and brittle propagation lines (red dashed arrows) have been marked for (**d**) as-machined and h) pre-charged specimens.

Table 6. Results of the fatigue test on AM-customized stainless steel.

Condition	Fatigue Life [Cycles]	Average Fatigue Life [Cycles]	Std. Deviation [Cycles]
As-machined [1]	2.8×10^5 3.8×10^5 5.0×10^5	3.9×10^5	1.1×10^5
Pre-charged for 360 h	3.9×10^5 6.2×10^5 4.1×10^5	4.8×10^5	1.3×10^5

[1] Pre-charging was not performed.

4. Discussion

The chemical composition of secondary-sourced metal was optimized to stabilize the austenitic phase without large deviations from the conventional compositional ranges of 316L stainless steel. As a result, an appreciable increment in the concentration of Cr, Ni, and Mo was reached, as reported in Table 2, and positively impacted on the mechanical properties of pre-charged specimens as demonstrated by the tensile and fatigue behavior of tested specimens. Indeed, higher concentrations of Ni and Mo have been conventionally considered to directly stabilize the austenitic phase of the stainless steel materials [9]. On the other hand, a higher Cr content has a double beneficial effect because it promotes the formation of protective oxide layers that function as a hydrogen permeation barrier, as well as giving superior resistance to generalized corrosion in the working environment [34]. Even though a direct comparison of the elemental concentrations of different stainless steel formulations is not possible, it is worth mentioning that the findings presented in this paper are well aligned with previous studies. Specifically, Bertsch et al. [21] presented a composition with a similar value for Ni_{eq} compared to this study—namely 31.79% compared to 30.98%—which yielded an overall resistance to HE under comparable parameters for the thermal hydrogen charging process.

Regarding the assessment of stainless steel performance, measurement of the hydrogen content, tensile tests, and fatigue tests were conducted as exhaustive methods to quantify the incorporation of hydrogen into the pre-charged specimens and then evaluate the effect of the incorporation of the mechanical response of the material to static and cyclic loads.

Concerning the static tensile properties, from the comparison of samples with and without pre-charging, it could be noted how the hydrogen incorporation impacted the strength of the material by moderately increasing both the yield and tensile strength. A more pronounced effect was detected for the specimens pre-charged for 360 h, as reported in Table 5. The reduction in elongation at fracture was consistent with the trend observed for strength, whereas the Reduction of Area showed changes in opposite directions for the samples pre-charged at 120 h and 360 h. Nevertheless, considering the uncertainties associated with the measurements, it could be noted that the difference between the properties of as-machined and pre-charged specimens are minor. Several approaches have been considered to generate metrics for HE of materials. The conventionally accepted figure is represented by the Relative Reduction of Area (RRA), calculated as the ratio of values of Reduction of Area of the specimen in the presence of hydrogen and in a reference environment (i.e., without hydrogen) [9]. Additionally, embrittlement indexes based on the relative loss of either the Reduction of Area or elongation at fracture have been

suggested [24]. With respect to the data presented in this study, the RRA parameter was calculated and resulted in values higher than 95% for both pre-charging conditions, whereas the loss of elongation at fracture was in the range of 10–20%, further supporting the observation that the newly developed material for AM is characterized by a significant resistance to HE compared to other stainless steel alloys reported in the scientific literature.

As observed by SEM and OM fractography on representative specimens for each test condition, the fracture surface of as-machined specimens was highly irregular and oval-shaped, with the core part characterized by the presence of dimples. The ratio between the maximum and minimum diameter was equal to 0.8235 mm/mm (Figure 4a,b). After pre-charging for 120 h, on the other hand, the fracture surface was less irregular, with a broader ductile region with the presence of dimples at the core of the sample, whereas flat and quasi-cleavage features were detected at the edges. The shape changed again from circular to elliptical, with a diameter ratio of 0.8450 mm/mm (Figure 4c,d). Finally, after pre-charging for 360 h, the fracture surface presented a higher fraction of quasi-cleavage features than the other two conditions. In this case, some of the laser scan tracks were still observable and the failure was most probably due to decohesion of the two adjacent printed layers. The shape of the specimen was affected the most, with the ratio of minimum and maximum diameters being 0.7692 mm/mm (Figure 4e,f). These observations were in accordance with the trends in variation in mechanical properties, implying that there might be a transition from ductile to brittle fracture by increasing pre-charging time.

Complementing the observations made on static properties, fatigue tests led to consistent conclusions. It was clear that no degradation was induced by hydrogen pre-charging during the HCF testing. Indeed, the resistance of the material exposed to hydrogen before the fatigue test was even improved compared to the as-machined conditions. Once again, to better understand the effect of hydrogen on fracture mode, the surfaces of the representative as-machined sample that failed at 5.0×10^5 cycles and the pre-charged sample that failed at 4.0×10^5 cycles were compared. The fracture surface of the as-machined sample (Figure 5a–d) was characterized by a crack initiation zone, a crack propagation zone, and a final fracture. The crack was triggered at a defect located near the surface (Figure 5b) and propagated, with clear marks from the propagation lines (Figure 5c) until the cross-section could not support the load. At that point, the fracture occurred in a ductile manner, as demonstrated by dimples observed in Figure 5d. Regarding the pre-charged specimen, similarly to the previous case, the fracture surface was characterized by a crack initiation zone, a propagation zone, and a final fracture. The crack was also initiated near a discontinuity in the material (Figure 5f), after which it advanced (Figure 5g) until the final ductile fracture occurred (Figure 5h). In this case, however, the propagation lines were more pronounced and were also present in the final fracture zone of the specimen, where only the dimples typical of ductile fracture should be visible. This could indicate the presence of secondary cracks due to the local stress state induced by molecular hydrogen, which may have begun to propagate inside the specimen to a certain extent during the test. However, for low-amplitude loads, these secondary cracks do not normally cause the specimen to fail and only become visible after the final fracture. Nevertheless, a more detailed analysis, with the use of fatigue testing coupled with tomographic analysis, would be required to confirm the hypothesis.

To balance the results presented in this paper with those from previous studies, it must be mentioned that degradation of fatigue properties due to HE in austenitic stainless steels have been extensively investigated for both conventionally manufactured and AM materials, comparatively to the same materials tested under the reference conditions without hydrogen charging [35–41]. Our findings on crack mode for pre-charged materials, although partially in contrast with previous studies on HCF behavior of 316L from

conventional manufacturing [36], are aligned with the previously reported outcomes for AM steels. In fact, an increased resistance to fatigue could be attributed to the combined effects of two factors. On the one hand, hierarchical microstructures resulting from the LPBF process may already hinder crack nucleation. Additionally, the modification of the chemical composition may contribute to the increase in the stability of austenite phase even under stress concentration, thus enhancing the resistance to fracture growth. Nevertheless, a comprehensive understanding of the impact of HE on the performance of austenitic steels under cyclic loads, normalized over several testing methods and parameters, is still lacking and further research is expected to close this knowledge gap.

5. Conclusions

A novel austenitic stainless steel with optimized chemical composition for hydrogen service was developed. Powders atomized from secondary-sourced metal were used as feedstock for the LPBF process to manufacture specimens, which were subsequently thermally charged with hydrogen and tested under static and cyclic loads. The analysis conducted with the following observations:

- Tuning of the chemical composition does not affect printability and yields high mechanical performance under both reference and pre-charged conditions.
- Thermal charging for 120 h and 360 h in a hydrogen-filled autoclave at 100 bar and 300 °C has a minor impact on the static tensile properties.
- Fatigue life for the specimens pre-charged for 360 h is improved with respect to the reference counterpart not exposed to hydrogen.

Potentially higher costs of production for the optimized alloy due to increased concentration of alloying elements, such as Ni and Mo, would be well compensated by improved mechanical performance. Moreover, the use of secondary-sourced material would also be beneficial to balance the total cost of production.

In conclusion, despite the observed minor changes in the mechanical properties of the material, the optimized formulation of the austenitic stainless steel allowed us to obtain promising mechanical performance, comparable to initial levels and in accordance with general standards for the application of AM 316L, thus suggesting that the AM material would demonstrate high stability during operation in hydrogen-rich environments.

6. Patents

Italian Patent N. 102021000024502 “Lega Metallica e Procedimento, particolarmente per la Realizzazione di Manufatti Idonei all’Impiego in Ambienti Esposti all’Idrogeno”, filing date 23/09/2021.

Author Contributions: Conceptualization, M.V., L.E.M. and M.G.; investigation, M.C., M.S.C., M.V., G.A. and F.E.; writing—original draft preparation, M.C. and M.S.C.; writing—review and editing, M.C., M.S.C., M.V. and F.E.; supervision, M.V., L.E.M. and M.G. All authors have read and agreed to the published version of the manuscript.

Funding: This research received no external funding.

Data Availability Statement: The original contributions presented in this study are included in the article. Further inquiries can be directed to the corresponding author(s).

Acknowledgments: The authors are grateful to Equinor ASA and IKM Flux AS for having provided the 316L scrap material, which was used for this project. The authors are thankful to Equinor ASA for the industrial support and the valuable insights.

Conflicts of Interest: The authors declare no conflicts of interest.

Abbreviations

The following abbreviations are used in this manuscript:

HE	Hydrogen Embrittlement
HEDE	Hydrogen-Enhanced Decohesion
HIPT	Hydrogen-Induced Phase Transformation
HELP	Hydrogen-Enhanced Local Plasticity
HESIV	Hydrogen-Enhanced Strain-Induced Vacancy
AIDE	Adsorption-Induced Dislocation Emission
AM	Additive Manufacturing
LPBF	Laser Powder Bed Fusion
VIM	Vacuum Induction Melting
VIGA	Vacuum Inert Gas Atomizer
ICP-OES	Inductively Coupled Plasma Optical Emission Spectroscopy
SEM	Scanning Electron Microscopy
PSD	Particle Size Distribution
OM	Optical Microscopy
UTS	Ultimate Tensile Stress
YS	Yield Stress
HCF	High Cycle Fatigue

References

1. Martins, F.P.; Almaraz, S.D.; Junior, A.B.; Azzaro-Pantel, C.; Parikh, P. Hydrogen and the sustainable development goals: Synergies and trade-offs. *Renew. Sustain. Energy Rev.* **2024**, *204*, 114796. https://doi.org/10.1016/j.rser.2024.114796.
2. Worku, A.K.; Ayele, D.W.; Deepak, D.B.; Gebreyohannes, A.Y.; Agegnehu, S.D.; Kolhe, M.L. Recent advances and challenges of hydrogen production technologies via renewable energy sources. *Adv. Energy Sustain. Res.* **2024**, *5*, 2300273. https://doi.org/10.1002/aesr.202300273.
3. Liu, J.; Zhao, M.; Rong, L. Overview of hydrogen-resistant alloys for high-pressure hydrogen environment: On the hydrogen energy structural materials. *Clean. Energy* **2023**, *7*, 99–115. https://doi.org/10.1093/ce/zkad009.
4. Bin, S.; Chen, Z.; Zhu, Y.; Zhang, Y.; Xia, Y.; Gong, S.; Zhang, F.; Shi, L.; Duan, X.; Sun, Z. High-pressure proton exchange membrane water electrolysis: Current status and challenges in hydrogen production. *Int. J. Hydrogen Energy.* **2024**, *67*, 390–405. https://doi.org/10.1016/j.ijhydene.2024.04.188.
5. Esfandiari, N.; Aliofkhazraei, M.; Colli, A.N.; Walsh, F.C.; Cherevko, S.; Kibler, L.A.; Elnagar, M.M.; Lund, P.D.; Zhang, D.; Omanovic, S.; et al. Metal-based cathodes for hydrogen production by alkaline water electrolysis: Review of materials, degradation mechanism, and durability tests. *Prog. Mater. Sci.* **2024**, *144*, 101254. https://doi.org/10.1016/j.pmatsci.2024.101254.
6. Patil, V.; Reshmi, P.V.; Prajna, S.; Haleshappa, D.; Jayarama, A.; Pinto, R. Degradation mechanisms in PEM fuel cells: A brief review. *Mater. Today Proc.* 2023, *in press*. https://doi.org/10.1016/j.matpr.2023.03.603.
7. Peng, J.; Zhao, D.; Xu, Y.; Wu, X.; Li, X. Comprehensive analysis of solid oxide fuel cell performance degradation mechanism, prediction, and optimization studies. *Energies* **2023**, *16*, 788. https://doi.org/10.3390/en16020788.
8. Lynch, S. Hydrogen embrittlement phenomena and mechanisms. *Corros. Rev.* **2012**, *30*, 105–123. https://doi.org/10.1515/corrrev-2012-0502.
9. San Marchi, C.; Somerday, B.P. *Technical Reference for Hydrogen Compatibility of Materials*; SAND2012-7321; Sandia National Laboratories: Albuquerque, NM, USA, September 2012. https://doi.org/10.2172/1055634.
10. Yu, H.; Díaz, A.; Lu, X.; Sun, B.; Ding, Y.; Koyama, M.; He, J.; Oudriss, A.; Feaugas, X.; Zhang, Z. Hydrogen Embrittlement as a Conspicuous Material Challenge—Comprehensive Review and Future Directions. *Chem. Rev.* **2024**, *124*, 6271–6392. https://doi.org/10.1021/acs.chemrev.3c00624.
11. Takakuwa, O.; Yamabe, J.; Matsunaga, H.; Furuya, Y.; Matsuoka, S. Comprehensive Understanding of Ductility Loss Mechanisms in Various Steels with External and Internal Hydrogen. *Metall. Mater. Trans. A* **2017**, *48*, 5717–5732. https://doi.org/10.1007/s11661-017-4323-3.
12. Takaki, S.; Nanba, S.; Imakawa, K.; Macadre, A.; Yamabe, J.; Matsunaga, H.; Matsuoka, S. Determination of hydrogen compatibility for solution-treated austenitic stainless steels based on a newly proposed nickel-equivalent equation. *Int. J. Hydrogen Energy* **2016**, *41*, 15095–15100. https://doi.org/10.1016/j.ijhydene.2016.06.193.

13. Gibbs, P.J.; Hough, P.D.; Thürmer, K.; Somerday, B.P.; San Marchi, C.; Zimmerman, J.A. Stacking fault energy based alloy screening for hydrogen compatibility. *JOM* **2020**, *72*, 1982–1992. https://doi.org/10.1007/s11837-020-04106-7.
14. Kim, M.-S.; Chun, K.W. A Comprehensive Review on Material Compatibility and Safety Standards for Liquid Hydrogen Cargo and Fuel Containment Systems in Marine Applications. *J. Mar. Sci. Eng.* **2023**, *11*, 1927. https://doi.org/10.3390/jmse11101927.
15. Fussik, R.; Egels, G.; Theisen, W.; Weber, S. Stacking Fault Energy in Relation to Hydrogen Environment Embrittlement of Metastable Austenitic Stainless CrNi-Steels. *Metals* **2021**, *11*, 1170. https://doi.org/10.3390/met11081170.
16. Lai, C.L.; Tsay, L.W.; Chen, C. Effect of microstructure on hydrogen embrittlement of various stainless steels. *Mater. Sci. Eng. A* **2013**, *584*, 14–20. https://doi.org/10.1016/j.msea.2013.07.004.
17. Barrera, O.; Bombac, D.; Chen, Y.; Daff, T.D.; Galindo-Nava, E.; Gong, P.; Haley, D.; Horton, R.; Katzarov, I.; Kermode, J.R.; et al. Understanding and mitigating hydrogen embrittlement of steels: A review of experimental, modelling and design progress from atomistic to continuum. *J. Mater. Sci.* **2018**, *53*, 6251–6290. https://doi.org/10.1007/s10853-017-1978-5.
18. Lee, J.C.; Yang, D.C.; Sung, M.Y.; Kim, N.S.; Park, H.K.; Choi, M.; Kim, Y.D.; Sohn, S.S.; Park, C.S. Influence of crystallographic textures on the hydrogen embrittlement resistance of austenitic stainless steel. *J. Mater. Res. Technol.* **2024**, *32*, 2757–2766. https://doi.org/10.1016/j.jmrt.2024.08.078.
19. Li, S.; Liu, M.; Ren, Y.; Wang, Y. Hydrogen embrittlement behaviors of additive manufactured maraging steel investigated by in situ high-energy X-ray diffraction. *Mater. Sci. Eng. A* **2019**, *766*, 138341. https://doi.org/10.1016/j.msea.2019.138341.
20. Alnajjar, M.; Christien, F.; Bosch, C.; Wolski, K. A comparative study of microstructure and hydrogen embrittlement of selective laser melted and wrought 17–4 PH stainless steel. *Mater. Sci. Eng. A* **2020**, *785*, 139363. https://doi.org/10.1016/j.msea.2020.139363.
21. Bertsch, K.M.; Nagao, A.; Rankouhi, B.; Kuehl, B.; Thoma, D.J. Hydrogen embrittlement of additively manufactured austenitic stainless steel 316 L. *Corros. Sci.* **2021**, *192*, 109790. https://doi.org/10.1016/j.corsci.2021.109790.
22. Yao, J.; Tan, Q.; Venezuela, J.; Atrens, A.; Zhang, M. Recent research progress in hydrogen embrittlement of additively manufactured metals—A review. *Curr. Opin. Solid State Mater. Sci.* **2023**, *27*, 101106. https://doi.org/10.1016/j.cossms.2023.101106.
23. Zhao, Q.; Luo, H.; Pan, Z.; Cheng, H.; Xu.; Duan, G.; Qin, Y.; Wang, G. Comparative study on hydrogen embrittlement resistance in additive manufactured and forged austenitic stainless steel. *Addit. Manuf.* **2024**, *88*, 104262. https://doi.org/10.1016/j.addma.2024.104262.
24. Nietzke, J.; Konert, F.; Poka, K.; Merz, B.; Sobol, O.; Böllinghaus, T. Comparison of hydrogen effects on additively manufactured and conventional austenitic steels. *Eng. Fail. Anal.* **2025**, *167*, 109042. https://doi.org/10.1016/j.engfailanal.2024.109042.
25. Zhou, C.; Yan, X.; Wang, H.; Huang, Y.; Xue, J.; Li, J.; Li, X.; Han, W. Advancements in hydrogen embrittlement of selective laser melting austenitic stainless steel: Mechanisms, microstructures, and future directions. *J. Mater. Sci. Technol.* **2025**, *230*, 219–235. https://doi.org/10.1016/j.jmst.2025.01.019.
26. Liu, J.; Yang, H.; Meng, L.; Liu, D.; Xu, T.; Xu, D.; Shao, X.; Shao, C.; Li, S.; Zhang, P.; et al. Significance of melt pool structure on the hydrogen embrittlement behavior of a selective laser-melted 316L austenitic stainless steel. *Materials* **2023**, *16*, 1741. https://doi.org/10.3390/ma16041741.
27. Claeys, L.; Deconinck, L.; Verbeken, K.; Depover, T. Effect of additive manufacturing and subsequent heat and/or surface treatment on the hydrogen embrittlement sensitivity of 316L austenitic stainless steel. *Int. J. Hydrogen Energy* **2023**, *48*, 36142–36157. https://doi.org/10.1016/j.ijhydene.2023.05.215.
28. International Organization for Standardization. ISO 13320:2020. Particle size analysis — Laser diffraction methods. Geneva: International Organization for Standardization; 2020. 59p. Available from: https://www.iso.org/standard/69111.html#lifecycle.
29. Advancing Standards Transforming Markets. ASTM B212-17 (2021). Standard Test Method for Apparent Density of Free-Flowing Metal Powders Using the Hall Flowmeter Funnel. West Conshohocken (PA): ASTM International; 2021. 4p. Available from: https://store.astm.org/b0212-17.html.
30. Advancing Standards Transforming Markets. ASTM B527-93 (2000). Standard Test Method for Determination of Tap Density of Metallic Powders and Compounds. West Conshohocken (PA): ASTM International; 2020. 2p. Available from: https://store.astm.org/b0527-93r00e01.html.
31. Advancing Standards Transforming Markets. ASTM B213-20 (2000). Standard Test Methods for Flow Rate of Metal Powders Using the Hall Flowmeter Funnel. West Conshohocken (PA): ASTM International; 2020. 4p. Available from: https://store.astm.org/b0213-20.html.
32. Advancing Standards Transforming Markets. ASTM E8/E8M-21 (2021). Standard Test Methods for Tension Testing of Metallic Materials. West Conshohocken (PA): ASTM International; 2021. 30p. Available from: https://store.astm.org/e0008_e0008m-21.html.

33. Advancing Standards Transforming Markets. ASTM E466-21 (2021). Standard Practice for Conducting Force Controlled Constant Amplitude Axial Fatigue Tests of Metallic Materials. West Conshohocken (PA): ASTM International; 2021. 7p. Available from: https://store.astm.org/standards/e466.
34. Kawami, K.; Kinoshita, A.; Yamanaka, H.; Fukuda, Y.; Enoki, H.; Iijima, T.; Fukuyama, S.; Tsukane, R.; Tanaka, T.; Fukutani, T.; et al. Evaluation of the Hydrogen Barrier Properties of Chromium Oxide Films Deposited on SUS304 Austenitic Stainless Steels. In Proceedings of the Pressure Vessels and Piping Conference, JW Marriott Las Vegas Resort & Spa, Las Vegas, NV, USA, 17 July 2022. https://doi.org/10.1115/PVP2022-80128.
35. Li, W.X.; Zhao, S.W.; He, P.F.; Wang, B.J. Experimental and numerical study on high-cycle fatigue performance of austenitic stainless steel with pre-charged hydrogen. *Int. J. Fatigue* **2024**, *185*, 108359. https://doi.org/10.1016/j.ijfatigue.2024.108359.
36. Zhao, C.; Deng, L.; Wu, S.; Wu, W.; Peng, Y.; Wang, X.; Jiang, Y.; Gong, J. Dual role of hydrogen in fatigue life of 316L austenitic stainless steel. *Int. J. Fatigue* **2025**, *198*, 108975. https://doi.org/10.1016/j.ijfatigue.2025.108975.
37. Behvar, A.; Haghshenas, M.; Djukic, M.B. Hydrogen embrittlement and hydrogen-induced crack initiation in additively manufactured metals: A critical review on mechanical and cyclic loading. *Int. J. Hydrogen Energy* **2024**, *58*, 1214–1239. https://doi.org/10.1016/j.ijhydene.2024.01.232.
38. Šmíd, M.; Koutný, D.; Neumannová, K.; Chlup, Z.; Náhlík, L.; Jambor, M. Cyclic behaviour and microstructural evolution of metastable austenitic stainless steel 304L produced by laser powder bed fusion. *Addit. Manuf.* **2023**, *68*, 103503. https://doi.org/10.1016/j.addma.2023.103503.
39. Gnanasekaran, B.; Song, J.; Vasudevan, V.; Fu, Y. Corrosion fatigue characteristics of 316L stainless steel fabricated by laser powder bed fusion. *Metals* **2021**, *11*, 1046. https://doi.org/10.3390/met11071046.
40. Zhu, H.; Pan, Q.; Zhang, K.; Zhou, C.; Zhang, W.; Yao, Y.; Ying, D.; He, Y.; Zheng, J.; Zhang, L. The difference in fatigue crack growth induced by internal and external hydrogen in selective laser melted 304L stainless steel. *Int. J. Fatigue* **2022**, *163*, 107052. https://doi.org/10.1016/j.ijfatigue.2022.107052.
41. Smith, T.R.; San Marchi, C.; Sugar, J.D.; Balch, D.K. Effects of extreme hydrogen environments on the fracture and fatigue behavior of additively manufactured stainless steels. In Proceedings of the Pressure Vessels and Piping Conference, Hyatt Regency San Antonio Riverwalk, San Antonio, TX, USA, 14 July 2019. https://doi.org/10.1115/PVP2019-93903.